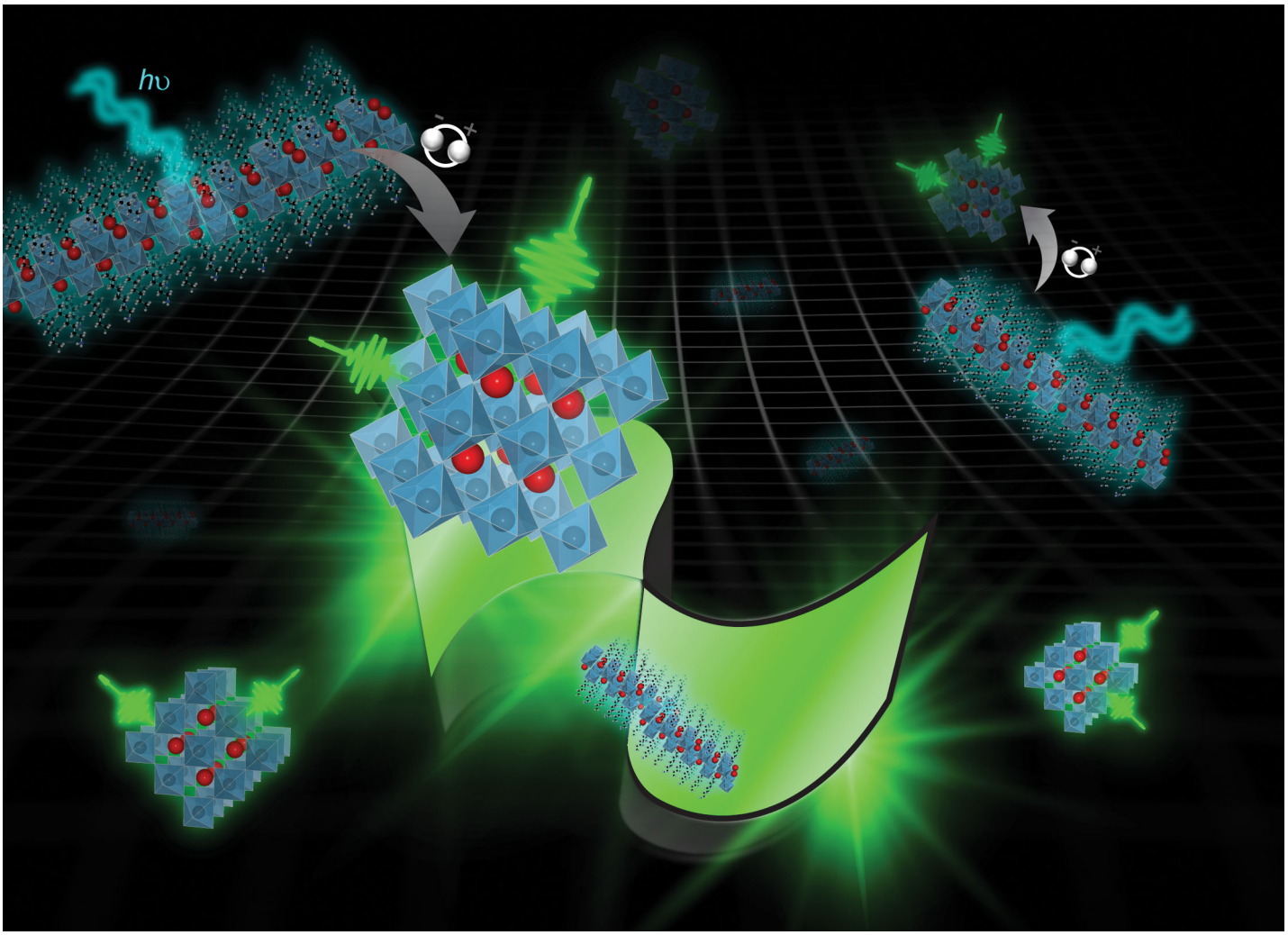

Showcasing collaborative research from Prof. Subodh Mhaisalkar's group at ERI@N (Singapore), Prof. Michael Grätzel's group at EPFL (Switzerland), and Prof. Henk Bolink's group at the University of Valencia (Spain).

Self-assembled hierarchical nanostructured perovskites enable highly efficient LEDs *via* an energy cascade

An innovative and easy to scale method to fabricate bright halide perovskite light-emitting diodes (LEDs) for large area illumination and displays applications is presented. We demonstrate a unique mesoscopic film architecture, based on the self-assembly of 2D octylammonium lead bromide platelets on 3D formamidinium lead bromide nanocrystals of graded size; enabling an energy cascade to yield bright and efficient LEDs with unprecedented performance metrics.

As featured in:

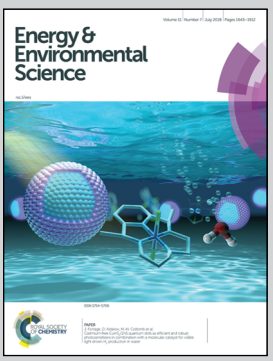

See Nripan Mathews, Subodh G. Mhaisalkar *et al.*, *Energy Environ. Sci.*, 2018, **11**, 1770.

ROYAL SOCIETY OF CHEMISTRY

rsc.li/ees

Registered charity number: 207890

Energy & Environmental Science

PAPER

View Article Online
View Journal | View Issue

Cite this: *Energy Environ. Sci.*, 2018, **11**, 1770

Self-assembled hierarchical nanostructured perovskites enable highly efficient LEDs *via* an energy cascade†

Xin Yu Chin,[a] Ajay Perumal,[b] Annalisa Bruno,[a] Natalia Yantara,[a] Sjoerd A. Veldhuis,[a] Laura Martínez-Sarti,[c] Bevita Chandran,[d] Vladimir Chirvony,[c] Alencious Shu-Zee Lo,[e] Jinkyu So,[e] Cesare Soci,[e] Michael Grätzel,[f] Henk J. Bolink,[c] Nripan Mathews *[ad] and Subodh G. Mhaisalkar *[ad]

Received 29th January 2018,
Accepted 12th March 2018

DOI: 10.1039/c8ee00293b

rsc.li/ees

Metal halide perovskites have established themselves as extraordinary optoelectronic materials, exhibiting promise for applications in large area illumination and displays. However, low luminescence, low efficiencies of the light-emitting diodes (LEDs), and complex preparation methods currently limit further progress towards applications. Here, we report on a new and unique mesoscopic film architecture featuring the self-assembly of 3D formamidinium lead bromide ($FAPbBr_3$) nanocrystals of graded size, coupled with microplatelets of octylammonium lead bromide perovskites, which enables an energy cascade, yielding very high-performance light-emitting diodes with emission in the green spectral region. These hierarchically structured perovskite films exhibit photoluminescence quantum yields of over 80% and LEDs associated with record high efficiencies in excess of 57.6 cd A^{-1} with an external quantum efficiency above 13%. Additionally, due to low turn-on voltages (~2.2 V) the LEDs have power efficiencies exceeding 58 lumens per watt, obtained without any light-outcoupling structures.

Broader context

Solution-processable halide perovskites have emerged as extraordinary optoelectronic materials for cost-effective and efficient photovoltaic applications and light-emitting diodes (LEDs). Despite major recent advances, the LED device efficiency is still lagging behind established technologies such as organic LEDs (OLEDs). The highest efficiencies reported to date are achieved by employing difficult-to-control anti-solvent engineering techniques to induce rapid crystallisation from solution; limiting the crystal growth while enhancing the radiative recombination properties. We propose to decouple the synthesis of nanocrystals from the film processing, allowing better control over the crystallite sizes and film morphology and an enhanced fabrication reproducibility. This can facilitate an improved scalability to larger area devices and high-throughput device printing methods. At the same time the hierarchically structured perovskite films obtained with this method have shown an external quantum efficiency exceeding 13% on small area devices and over 12% on large scale devices. These are amongst the highest reported values at the moment. This work thus presents an innovative and easy to scale method to fabricate bright and extremely efficient halide perovskite LEDs for potential applications in large area illumination and displays.

[a] *Energy Research Institute at Nanyang Technological University (ERI@N), 50 Nanyang Drive, Research Techno Plaza, X-Frontier Block, Level 5, Singapore 637553, Singapore. E-mail: nripan@ntu.edu.sg, subodh@ntu.edu.sg*
[b] *Department of Physics, Indian Institute of Science Education and Research (IISER), Berhampur, Odisha, 760010, India*
[c] *Instituto de Ciencia Molecular, Universidad de Valencia, C/Cat. J. Beltran 2, 46980 Paterna, Spain*
[d] *School of Materials Science and Engineering, Nanyang Technological University, Singapore, 639798, Singapore*
[e] *Centre of Disruptive Photonics Technologies, Division of Physics and Applied Physics, School of Physical and Mathematical Sciences, Nanyang Technological University, Singapore, 637371, Singapore*
[f] *Laboratory of Photonics and Interfaces, Department of Chemistry and Chemical Engineering, Swiss Federal Institute of Technology, Station 6, Lausanne 1015, Switzerland*

† Electronic supplementary information (ESI) available. See DOI: 10.1039/c8ee00293b

Metal halide perovskites have emerged as the only solution-processable photovoltaic technology to outperform multicrystalline silicon, by virtue of its intrinsic properties such as large absorption coefficient, balanced charge carrier transport, highly crystalline film formation, weak exciton binding energies, and slow bimolecular recombination.[1] Since 2014, perovskites have made strides in light-emitting applications with the first demonstration of amplified spontaneous emission and LEDs.[2,3] LEDs comprising various perovskite compositions have been reported, with a vast majority describing LEDs with low efficiency and luminance.[4–6] Central to the below-par efficiency have been low photoluminescence quantum yields (PLQYs) in the films resulting from the low exciton binding energies in 3D perovskites

(*e.g.* $CH_3NH_3PbBr_3$) and consequently slow electron–hole bimolecular recombination rates, especially at low carrier injection regimes where typical LEDs operate. High carrier density regimes where the PLQY could be higher, typically lead to material degradation.[3,7–10]

In the typical LED operational regime, the charge carrier concentrations ($\sim 10^{15}$ cm^{-3}) are comparable to the trap densities in 3D perovskites, which in combination with the large diffusion lengths (and charge carrier delocalization) leads to strong trap-mediated non-radiative recombination effects.[8,11] Strategies to counter these limitations include ultrathin emitter layers, nanostructured materials, grain size control through additives and process control (which localize the injected carriers), and the formation of low-dimensionality layered-perovskites (primarily modulating the excitonic effects). While the first PeLEDs were only demonstrated in 2014, the field evolved rapidly beyond 10% EQE, largely due to fast adaption of sequential advances in the field of QLEDs and organic LEDs; in which record EQEs in excess of 27% and 31% are demonstrated, respectively.[12,13] A solvent engineering approach led to $MAPbBr_3$ nanograins ($\sim$100 nm grains) with a maximum external quantum efficiency (EQE) of 8.5% and efficiencies of $\sim$43 cd A^{-1}, with the enhanced performance attributed to increased radiative recombination rates in nanoparticles or small crystal domains.[4] Long-chain ammonium halide surfactants provide surface passivation and limit the grain sizes to under 10 nm, resulting in an enhanced EQE of 10.4%.[8] In quasi-2D or Ruddlesden–Popper perovskites with a PLQY of $\sim$70%, improved LED performances, and an EQE of 11.7%,[14] have been attributed to an energy funnelling mechanism related to the presence of domains exhibiting a range of energetic excited states, enabling spatial concentration and confinement of excitons and high electroluminescence. These quasi-2D systems show promising performance and could still be improved by increasing the concentration of the emitting 3D perovskite domains in the thin films. Fabrication processes described thus far, involve precise control over surfactant addition and sensitive post-processing procedures, unfavourable to concerted commercialisation efforts. Decoupling the synthesis of perovskite nanocrystals (NCs) from the thin film processing step would allow for better control over crystal size and film thickness, thus improving fabrication reproducibility and advancing opportunities for scaling up device fabrication. Typically, long-chained capping ligands are employed during the NC synthesis to restrict the growth of the NCs and ensure colloidal stability of the solution.[15,16] Despite providing good surface passivation, these long chain ligands limit the electrical

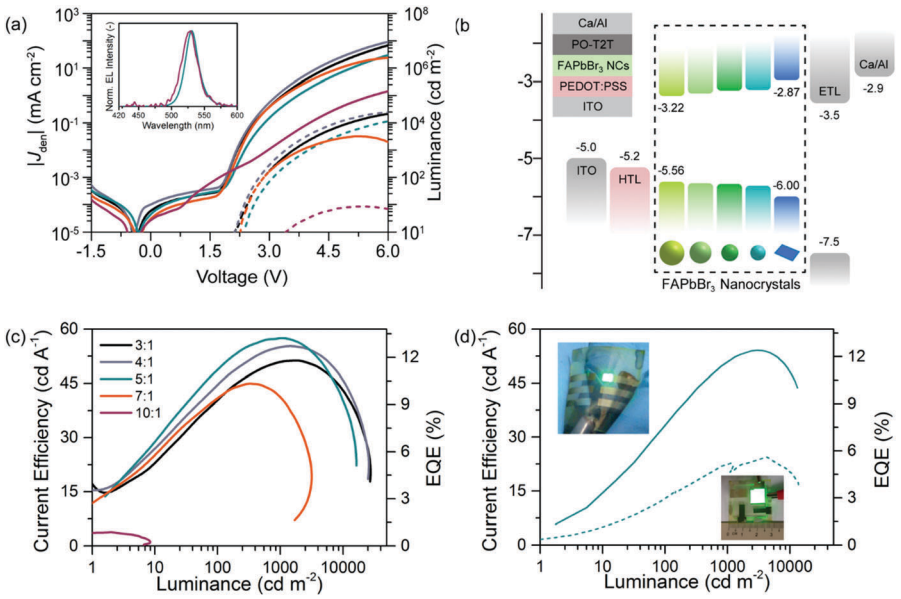

Fig. 1 Device characteristics of LEDs. (a) Current–voltage–luminance characteristics of NC LEDs. The inset shows the electroluminescence spectra of the respective devices. The EL peak is positioned around 528–532 nm with a FWHM of *ca.* 25–26 nm, corresponding to CIE 1931 colour coordinate (0.20, 0.76). Black, grey, dark cyan, orange, and purple curves show NCs with molar ratios of 3 : 1, 4 : 1, 5 : 1, 7 : 1, and 10 : 1 of OA : $PbBr_2$, respectively. (b) Schematic band diagram of the NC LEDs used in this work. (c) Characteristic current efficiency/EQE *versus* luminance (device area: 3 mm^2). (d) Current efficiency/EQE *versus* luminance of flexible (3 mm^2) and large area (95.2 mm^2) LED devices, with 4 : 1 NCs.

Table 1 The maximum luminance, current efficiency, luminous power efficiency, and EQE of the LED devices (as depicted in Fig. 1)

OA : $PbBr_2$ [—]	No. of devices [—]	Luminance [cd m^{-2}]	Current efficiency [cd A^{-1}]	Luminous power efficiency [lm W^{-1}]	EQE [%]
3 : 1	20	36 349 (32 030)	51.3 (33.0)	46.8 (28.2)	12.0 (7.8)
4 : 1	49	56 143 (33 054)	55.5 (52.7)	58.1 (51.3)	12.9 (12.3)
5 : 1	34	34 480 (21 354)	57.6 (52.5)	51.7 (46.1)	13.4 (12.1)
7 : 1	23	3325 (2359)	45.0 (41.0)	45.7 (40.3)	10.5 (9.6)
10 : 1	14	8.4 (6.4)	5.4 (2.9)	4.8 (2.6)	1.5 (0.8)

injection into the perovskite layer due to their insulating nature. A methodology that would allow for precise nanoparticle synthetic control and assembly to form highly efficient emitter layers is a requisite for a breakthrough in device performance.

Herein, we present high-performance devices fabricated from a synthetic protocol comprising judicious control over the addition of ligands to formamidinium bromide (FABr) and $PbBr_2$, to form a hierarchical self-assembly of 2D octylammonium lead bromide microplatelets ($(OA)_2(FA)_{n-1}Pb_nBr_{3n+1}$ MPLs) and $FAPbBr_3$ NCs (see Materials and methods for details). The self-assembled mesoscopic thin films comprising large plate-like ($\sim$0.5–2 μm edge length) domains of $(OA)_2(FA)_{n-1}Pb_nBr_{3n+1}$ and $FAPbBr_3$ NCs were sandwiched between suitable electron and hole transporting layers yielding the highest combination of EQE, luminance, power and current efficiency values (13.4% EQE, $\sim$56k cd m^{-2}, 58.1 lm W^{-1}, 57.6 cd A^{-1}) demonstrated to date in green-emitting perovskite LEDs.

The excellent quality of the diodes with the different OA : $PbBr_2$ ratios (Fig. 1, Fig. S1 and Table S1, ESI†) is evidenced by the low leakage current (<1 μA cm^{-2}) and the sharp turn-on of both the current density and luminance around 2.2–2.4 V. Device performance statistics (of 20–50 devices under each synthetic condition) show excellent reproducibility within the range of 4 : 1 and 7 : 1 OA : $PbBr_2$ ratios (Table 1, Fig. 2, Fig. S2, S3 and Tables S2, S3, ESI†). This validates the benefit of preparing and isolating the perovskite components prior to the integration into thin film devices. The correct choice of electron transport layer was essential to achieve charge balance and thus high efficiencies (Fig. S4, S5 and Table S4, ESI†). Indeed, the use of PO-T2T (2,4,6-tris[3-(diphenylphosphinyl)phenyl]-1,3,5-triazine), as opposed to B3PYMPM (4,6-bis(3,5-di(pyridin-3-yl)-phenyl)-2-methylpyrimidine), as an electron transporting layer of the LED devices lowered the turn-on voltage and improved the luminance, luminous power efficiency, current efficiency, and EQE. We attribute the overall improvement to the better hole-blocking properties of PO-T2T, enabled by the deeper HOMO level of PO-T2T (-7.5 eV)[17] compared to -6.9 eV of B3PYMPM[18] (Fig. S7, ESI†), while the reduction in the turn-on voltage is likely related to the superior electron mobility of PO-T2T ($\sim10^{-3}$ cm^2 V^{-1} s^{-1})[19] *versus* B3PYMPM ($\sim10^{-4}$ cm^2 V^{-1} s^{-1}).[20] These optimised devices displayed uniform and bright green emission (Fig. S6, ESI†), a fair temporal stability (Fig. S7, ESI,† comparable to the best efficiency PeLEDs[7,11,21]), and stable colour emission (Fig. S8, ESI†). Moreover, an excellent repeatability of device metrics (*i.e.* luminance and efficiency) was also achieved across a wide range of measurement scan rates (in the range 0.1–2 V s^{-1}), indicating minimal defects across the active layers and interfaces. These excellent properties allowed the conversion into flexible devices (3 mm^2, 12.4% EQE, $>$13k cd m^{-2}) and large-area devices (up to 95.2 mm^2, 5.7% EQE, $>$13k cd m^{-2}) as presented in Fig. 1d, Fig. S10, S11 and Tables S5–S8 (ESI†).

To elucidate the transport properties of the perovskite active layers, we collected current–voltage characteristics of single-carrier devices. In the case of the electron-only devices (device stack: ITO/PEIE/Perovskite/PO-T2T/Ca/Al, Fig. 3a), PEIE-treated

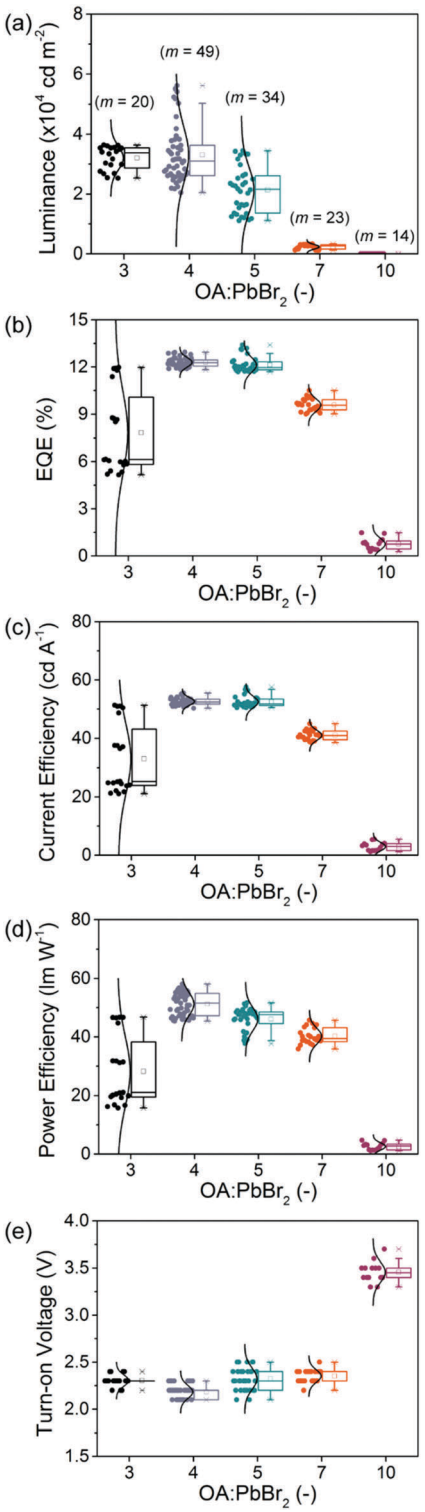

Fig. 2 Device statistics of LEDs. (a) Luminance, (b) EQE, (c) current efficiency, (d) power efficiency, and (e) turn-on voltage values shown as box plots for LED devices (*m* is the number of devices measured) based on different OA : $PbBr_2$ ratios. Each measured device is represented by filled circles with a normal distribution. The squares and crosses represent the median values and outliers, whereas the error bars represent the minimum and maximum values. Lower and upper bars within the box, represent the first and third quartile (Q1 and Q3), respectively.

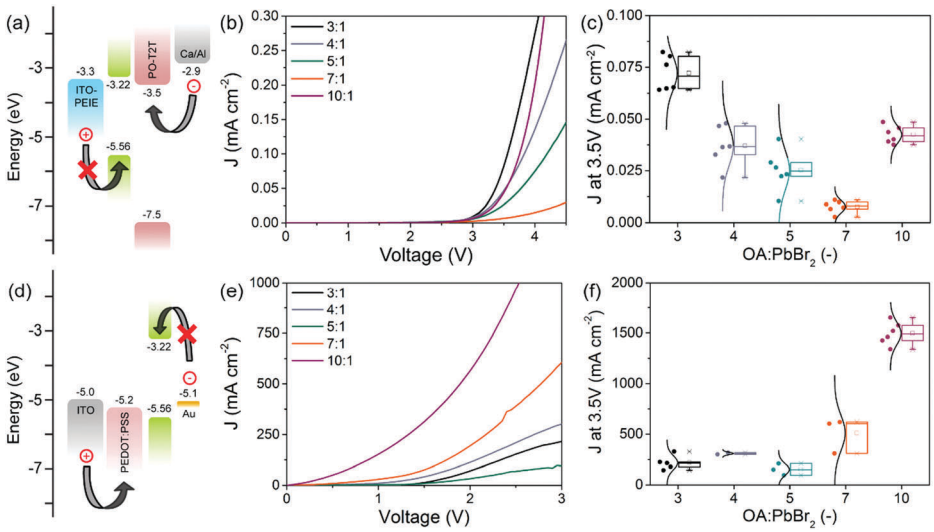

Fig. 3 Single carrier devices fabricated with different OA : $PbBr_2$ ratios. (a and d) Band diagrams, (b and e) representative *J*–*V* curves, and (c and f) box plots of the current density for electron-only (at 3.5 V) and hole-only (at 3.5 V) devices, respectively.

ITO substrates (work function 3.3 eV) were used instead of ITO/PEDOT:PSS, to block the hole injection into the perovskite layer. Conversely, for the hole-only devices (device stack: ITO/PEDOT:PSS/Perovskite/Au, Fig. 3d) we employed a Au contact, rather than PO-T2T/Ca/Al, to create a barrier for electron injection into the perovskite layer. The current density–voltage characteristics and current at 3.5 V for electron-only devices are summarized in Fig. 3b and c, which show that upon increasing the OA : $PbBr_2$ ratios (up to 7 : 1), the electron-transport in the devices decreases. On the other hand, hole injection (Fig. 3e and f) appears independent of the OA : $PbBr_2$ ratios up to 7 : 1. When OA : $PbBr_2$ is 10 : 1, significantly enhanced electron- and hole-transport was observed for all tested devices, presumably caused by pin holes in the resulting perovskite thin films (*i.e.* electrical shunt paths), as observed in the topographical images (see Fig. S15, ESI†). We note that no EL is observed in the single-carrier devices at higher operating voltages (*ca.* 3–4 V), suggesting that the diodes are operating with negligible minority carriers in the investigated operating regime. The balance between electron- and hole-injection into the emitter film is altered by the reduction of electron transport at increased OA : $PbBr_2$, which affects the device efficiency. The highest device efficiencies were achieved using 4 : 1 and 5 : 1, inferring more balanced carrier injection in these devices.

Although the efficiencies of the devices are high, the devices suffer an efficiency droop at higher current density, *i.e.* drop of efficiency at high luminance or in the high current density regime. The drop of efficiency in perovskite LEDs has previously been observed and attributed to the heat degradation of the materials driven at a large current density, where luminescence stability is observed to be improved while operating the LED with short duration voltage pulses.[3] It should also be noted that an efficiency droop is also commonly observed in nitride-based LEDs, where heat degradation,[22] enhanced Auger recombination,[23] carrier overflow at high carrier population,[24–26] and a carrier delocalization effect[27] have been argued to be the possible mechanism behind the unwanted phenomenon. The exact mechanism of the efficiency droop for PeLEDs is at present not completely understood and more investigations are required to resolve this issue.

As evidenced by field-emission scanning electron microscopy (FESEM), transmission electron microscopy (TEM), and cathodoluminescence (CL) studies, preferential deposition of the micron-sized 2D MPLs is observed on top of the 3D NCs, while the ratio between the 2D MPLs and 3D NCs can be conveniently modulated by varying the OA : $PbBr_2$ ratio. This self-assembly is induced by complete wetting of the substrate's surface, prior to spin-coating. Here, the 2D MPLs arguably accumulate at the liquid–air interface due to their large ligand-to-surface ratio (*i.e.* similar to Langmuir–Blodgett), and the yielded films are very smooth (RMS ± 1 nm) mesoscopic composites (Fig. 4a, b and Fig. S12–S15, ESI†) consisting of rectangular (or polygonal) MPLs intimately in contact with NCs of graded particle sizes (~5–30 nm). Morphological images of the films prove the formation of uniform and compact films. Only for thin films fabricated with OA : $PbBr_2$ 10 : 1 agglomerated structures were formed, indicating appropriate usage of surface ligands at lower ligand-to-precursor ratios. In SEM top view images (Fig. S12, ESI†) an increasing number of micrometer-sized dark patches were observed on the film's surface at increasing OA : $PbBr_2$ ratios. This can be related to the existence of $(OA)_2(FA)_{n-1}Pb_nBr_{3n+1}$ MPLs as revealed by the CL mapping (Fig. S22, ESI†). In addition, the number of MPLs on the surface could be maximised by increasing the delay times between dropping of the NC ink and the spin coating step (Fig. S13, ESI†). The current distribution throughout the film was observed using conducting AFM at 1 V bias (Fig. S15, ESI†). Uniform current was observed across the 3 : 1, 4 : 1, 5 : 1, and 7 : 1 films. This indicates that the existence of 2D MPLs does not significantly hinder the current flow at these compositions. In the case of the 10 : 1 film,

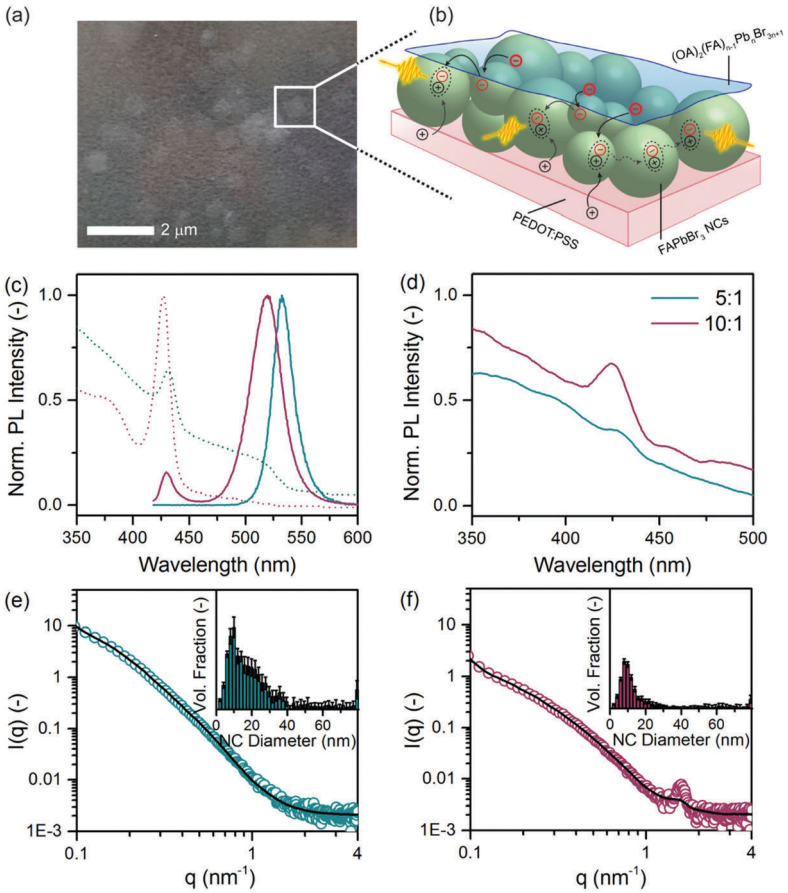

Fig. 4 Optical and structural characterisation of mixed $FAPbBr_3$ NCs and $(OA)_2(FA)_{n-1}Pb_nBr_{3n+1}$ MPLs. (a) The top-view FE-SEM image. (b) Schematic illustration of energy transfer under LED device operation in the deposited NCs thin film on top of PEDOT:PSS. (c) Absorption and steady-state photoluminescence (λ_{ex} = 405 nm) spectra showing excitonic absorption and photoluminescence from $(OA)_2(FA)_{n-1}Pb_nBr_{3n+1}$, for OA : $PbBr_2$ is 5 : 1 (dark cyan) and 10 : 1 (purple). (d) Excitation spectra (λ_{em} = 533 and 519 nm, for 5 : 1 and 10 : 1, respectively). (e and f) Small-angle X-ray scattering (SAXS) curves of NC inks, showing a Bragg reflection of the 2D MPLs. Insets: Particle size distribution extracted from the scattering curves.

patches of higher resistance area were noticed, which could be related to the existence of 2D MPL agglomerates, in agreement with the topographical images of the film (Fig. S12, ESI†).

Detailed characterisation by means of absorption and photoluminescence spectroscopy and small-angle X-ray scattering (SAXS), and X-ray diffraction (Fig. 4c–f and Fig. S16–S19, ESI†) indicate the presence of 2D $(OA)_2(FA)_{n-1}Pb_nBr_{3n+1}$ MPLs and 3D $FAPbBr_3$ NCs with a narrow size distribution of preferred orientation parallel to the substrate's surface. The steady state optical absorption spectra (Fig. 4c and Fig. S16, ESI†) of NC thin films with 5 : 1 and 10 : 1 OA : $PbBr_2$ ratios indicate the presence of two main features, a peak at 440 nm (*ca.* 2.82 eV) that corresponds to the excitonic absorption of the 2D MPLs and the band absorption of 3D $FAPbBr_3$ NCs at 520–530 nm (*ca.* 2.38–2.34 eV). The peak intensity consistently changes with the OA content due to the increased presence of $(OA)_2(FA)_{n-1}Pb_nBr_{3n+1}$ MPLs with respect to $FAPbBr_3$ NCs. The PL spectra show a pronounced emission from the MPLs at ~440 nm (for the 10 : 1 composition), however this emission is markedly absent from the 5 : 1 PL spectra. Excitation spectra (λ_{em} = 533 and 519 nm, for 5 : 1 and 10 : 1, respectively) provide the first intimation of an energy cascade from the higher bandgap $(OA)_2(FA)_{n-1}Pb_nBr_{3n+1}$ MPLs to the lower bandgap $FAPbBr_3$ NCs through a PL contribution around 425–430 nm (Fig. S17c, ESI†).

The presence of composite 2D and 3D perovskite structures was further confirmed by SAXS and XRD patterns with Bragg reflections of 2D $(OA)_2(FA)_{n-1}Pb_nBr_{3n+1}$ MPLs at $q \sim 1.60\ nm^{-1}$ (d-spacing of ~3.93 nm) and 2θ = 8–12°, respectively, at OA : $PbBr_2$ = 10 : 1; and predominance of the 3D $FAPbBr_3$ NCs at lower OA : $PbBr_2$ ratios.

Particle size distributions extracted from the SAXS scattering curves elucidate that the films are made up of NCs with a median diameter around 10 nm; with a narrower distribution for samples with OA : $PbBr_2$ ratios of 5 : 1 and with a much wider distribution at higher ratios (refer to Fig. S18, ESI† for details). Rocking curves of (001) reflection of $(OA)_2(FA)_{n-1}Pb_nBr_{3n+1}$ (2θ: ~9.6°) and (002) reflection of $FAPbBr_3$ (2θ: ~29.8°), display the occurrence of a peak, indicating a preferred orientation of both phases through self-assembly (refer to Fig. S17, ESI† for details).

Grazing-incidence small-angle X-ray scattering (GISAXS) was employed to probe the microstructural changes of the surface layer as a function of the delay time between drop casting of the NC inks and the subsequent spin-coating step (Fig. S18 and S19, ESI†).

While the lateral sizes of the MPLs are greater than observable in the measured q-range, Bragg-like reflections are only observed in samples prepared with OA : $PbBr_2$ = 10 : 1 at 2.23 and 2.50 nm^{-1} (Fig. S19d–f; also for OA : $PbBr_2$ = 7 : 1 in Fig. S18d, ESI†). The corresponding interlayer distances of *ca.* 28.2 and 25.1 Å, respectively, do not match the observed lattice spacing for pure $(OA)_2PbBr_4$,[28] but rather signify a persistent average distance between a multiple of stacked MPLs parallel to the substrate's surface. The further appearance of a 'bump' at $q \sim 1.85$ nm^{-1} (*i.e.* ~34 Å spacing) after 5 min delay further implies that this self-assembly into hierarchically stacked structures is a dynamic process. This is corroborated by the XRD measurements showing that the diffraction peak at $2\theta \sim 9.6^\circ$ moves to lower angles (Fig. S17a, ESI†). The absence of Bragg-like features in samples prepared with OA : $PbBr_2$ < 5 : 1 (Fig. S18f–h and S19a–c, ESI†) can be explained by the limited scattering volume of the MPLs (*i.e.* due to their low concentration on the surface). However, from the data obtained from SEM (Fig. S12 and S13, ESI†) and XRD (Fig. S17, ESI†) we infer that these MPLs are present.

Through a combination of transient optical spectroscopic techniques, we elucidate the energy cascade mechanism taking place from high bandgap 2D $(OA)_2(FA)_{n-1}Pb_nBr_{3n+1}$ MPLs into progressively lower bandgap $FAPbBr_3$ NCs, giving rise to high luminescence efficiency in $FAPbBr_3$ NC LEDs. Indeed, when charge carriers are injected (or photons are absorbed) into the 2D MPLs, since the energy transfer is fast enough to overcome non-radiative recombination, the excitons are preferentially transferred to the energetically favoured lower bandgap 3D $FAPbBr_3$ NCs, as in other multi-domain systems.[7,18–20,29] As a consequence, the photoexcited states tend to concentrate in the lower bandgap NCs, where the higher exciton concentrations would enhance the bimolecular radiative recombination.

The TA change following a λ = 375 nm pulsed excitation reveals two strong bleaching features at 440 and 520 nm for the 5 : 1 sample, in agreement with the absorption spectra (Fig. 5a, central and upper panels). The TA spectrum for the 10 : 1 panel is dominated by the photobleaching peak at 440 nm, indicating that the excitons are predominantly formed in the $(OA)_2(FA)_{n-1}Pb_nBr_{3n+1}$ MPLs. A secondary, albeit less intense peak at 520 nm, is detected and displays a rapid peak shift from 500 to 525 nm within 1 ps. The relative intensities of these two peaks are in agreement with the peaks in the absorption spectra for both samples. The 440 nm component is much shorter lived with respect to the 520 nm peak; the latter still observable even after 1000 ps (Fig. 5a and b lower panel).

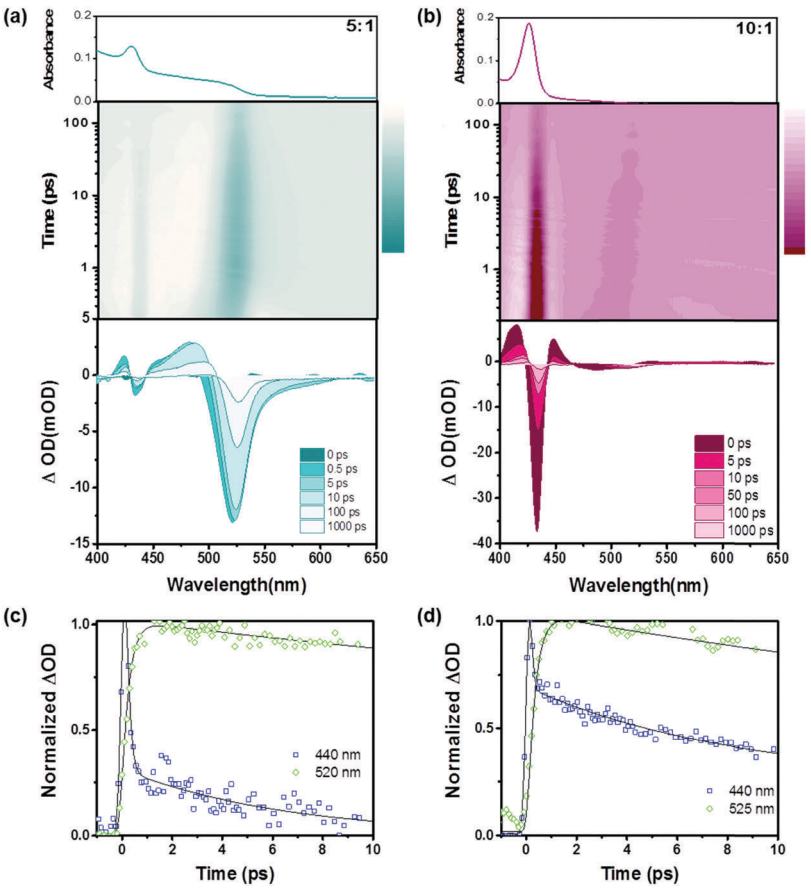

Fig. 5 Transient absorption (TA) spectra of $FAPbBr_3$ NCs. (a and b) UV-Visible absorption spectra (top) panel. TA mapping with excitation at λ = 375 nm, 150 fs, and 1 μJ cm^{-2} fluency in the 0–200 ps range (central panel) and the relative TA spectra up to 1000 ps (lower panel) for $FAPbBr_3$ NCs prepared with 3 : 1 (a), 4 : 1 (b) and 7 : 1 (c) OA : $PbBr_2$. Normalised kinetics of the TA signal at 440 nm and 520 nm for $FAPbBr_3$ NCs prepared with 5 : 1 (c) and 10 : 1 (d) OA : $PbBr_2$.

The kinetics of the TA signal at 440 nm and 525 nm for the 5 : 1 and 10 : 1 samples (Fig. 5c and d) provide strong evidence of an energy cascade between the $(OA)_2(FA)_{n-1}Pb_nBr_{3n+1}$ MPLs and $FAPbBr_3$ NCs. The 440 nm TA kinetics display very fast rising times, indistinguishable from the response function even after deconvolution (~150 fs), compatible with photon absorption taking place in the $(OA)_2(FA)_{n-1}Pb_nBr_{3n+1}$ MPLs. In contrast, the 520 nm kinetics display much slower (~400 fs) rise times, indicating a slower build-up of the absorption signal in $FAPbBr_3$ NCs, due to an energy cascade from the higher bandgap 2D MPLs to the lower bandgap $FAPbBr_3$ NCs.[11] The hierarchical architecture thus produces a vectoral energy flow within the self-assembled mesoscopic structure that enables the diodes to operate as very efficient light emitters. Subsequently, the $FAPbBr_3$ exciton population grows from the energy transfer, while its decay is dominated by radiative recombination. For all $OA : PbBr_2$ ratios, the decay kinetics at 525 nm are slower than that for 440 nm (refer to Fig. S20, S21; and Table S9, ESI† for details).

To visualize the emission from $FAPbBr_3$ NCs and $(OA)_2(FA)_{n-1}Pb_nBr_{3n+1}$ MPLs locally, CL mapping was used (Fig. 6a and Fig. S22, ESI†). Here, a striking enhancement of green emission (at 525 nm) was observed for $FAPbBr_3$ NCs existing in the vicinity of 2D MPLs. Only when the emission was filtered to exclude the green signal could the 440 nm emission from the MPLs be discerned (its relative intensity was very low due to fast energy transfer) (Fig. S23, ESI†). PL lifetimes probed between 440 and 540 nm (λ_{ex} = 405 nm) showed a significant spread consistent with graded NC sizes (*ca.* 5–30 nm) (Fig. 6b). Moreover, when excitons form in the higher bandgap (*i.e.* smaller NCs) and rapidly cascade into the lowest bandgap larger NCs within the size distribution, a variation in the relative weight of the components (of their corresponding PL life-times) is expected. At shorter probing wavelengths, the measured bi-exponential decay is dominated by a fast component related to intraband relaxation pathways inducing carrier cascading, whereas the largest $FAPbBr_3$ NCs (*i.e.* probed at longer wavelengths) show

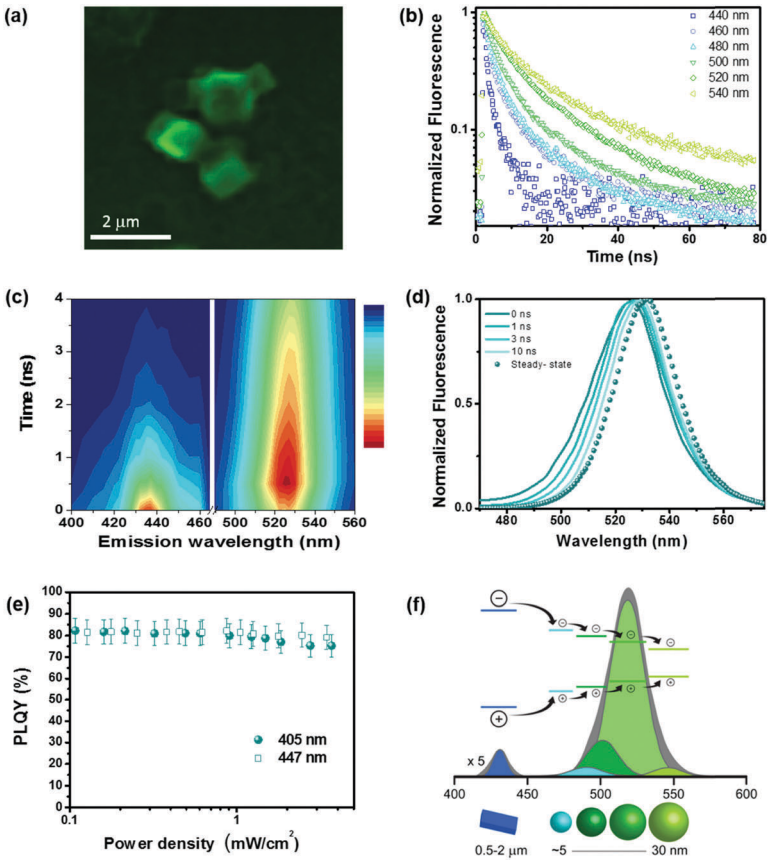

Fig. 6 Emission properties of hierarchically structured films prepared with $OA : PbBr_2$ = 5 : 1. (a) Cathodoluminescence image of a spin-coated film on a silicon substrate. Images are taken using an electron beam of 5 keV energy, current of ~11 nA, and exposure time of 10 ms. The image is obtained by mapping with an emission wavelength at 525 nm. (b) Time-resolved fluorescence decays collected at different emission wavelengths from 440 nm to 540 nm (blue square and slight green left-pointing triangle, respectively) at λ_{ex} = 405 nm. (c) Transient PL spectra at a time interval from 0–4 ns. (d) Normalised transient PL spectra at different time delays after excitation and the steady-state PL spectrum. (e) PLQY *versus* power density after CW laser excitation at λ = 405 and 447 nm. (f) Conceptual diagram representing the energy cascade from 2D MPLs to $FAPbBr_3$ NCs of graded size, where the deconvolution of the steady-state PL spectrum clearly displays the different PL contribution at varying NC sizes. Note: Deconvolution of the PL spectrum into 4 Gaussians is only used to illustrate the energy cascading from the smallest to largest NCs (*i.e.* largest to smallest bandgap). It does not represent the distribution of discrete energy levels originating from a continuous distribution of NCs of *ca.* 5–30 nm diameter, as extracted from the SAXS curves (Fig. S18, ESI†).

considerably longer lifetimes, where bimolecular recombination is the predominant process. (Tables S10–S14, ESI†). Additionally, from transient photoluminescence spectra (Fig. 6c) we can discern the ultrafast build-up of the emission at 440 nm and its rapid decay (within hundreds of picoseconds), which corroborates well with our previous TA observations (Fig. 5a and b). Conversely, the emission associated with the NCs (*ca.* 525 nm) only reached maximum emission after 500 ps, which confirms that the delayed build-up is owing to the energy cascade. This effect was further highlighted by the progressive red-shift of the emission peak within 10 ns (from 525 to 530 nm) (Fig. 6d), and a steady-state emission at 532 nm. The concurrent dynamic changes in the spectral shape and decreasing FWHM are thus likely caused by the lower contribution of the smallest NCs (*i.e.* blue-shifted part of the spectra), and associated with the energy cascade from the higher-to-lower bandgap. Consequently, this results in the narrowing of the transient emission spectra at longer decay times, eventually culminating in an even narrower steady-state emission (Fig. 6d).

PLQY of the composite films in the low power density regime (up to 6 mW cm^{-2}) recorded values of 80% consistently for both λ_{ex} = 405 nm (*i.e.* 2D MPLs and 3D NCs are excited) and λ_{ex} = 447 nm (*i.e.* 2D MPLs are not excited) (Fig. 6e; refer to Fig. S24 (ESI†) for additional details of PLQY as a function of λ_{ex}, power density, and OA : $PbBr_2$ ratios). The invariance of PLQY as a function of power density indicates that owing to the energy cascade mechanism, the carrier densities in the NCs have increased to a point whereby the trap states are overwhelmed and the chances of non-radiative recombination effectively suppressed; thus delivering a near unity value in photoluminescence yields. Concomitantly, the similar high PLQY values obtained at different excitation wavelengths further confirm that efficient energy transfer allows all absorbed photons (by the 2D MPLs) to be transferred as excitons in the graded $FAPbBr_3$ NCs.

The concept of multiple contributions from differently-sized NCs (as extracted from the scattering curves; *ca.* 5–30 nm) on the overall PL emission, is illustrated by deconvolution of the PL spectrum (Fig. 6f). This is confirmed by the considerable spread of characteristic lifetimes within the emission peak (Fig. 6b). The LED performance depends on the OA : $PbBr_2$ ratio, and in correlation with PLQY, drops for films with ratios above 5 : 1. As the amount of octylamine increases (to 10 : 1), the fraction of 2D MPLs increases, and the device efficiency decreases owing to factors including poor charge injection/transport and increased roughness of the films (Fig. 2 and Fig. S12, S15, ESI†). Emitters based on OA : $PbBr_2$ ratios of 3 : 1, 4 : 1 and 5 : 1 display good LED performances in line with the high PLQY observed for these films.

Conclusions

We developed 2D–3D self-assembled hierarchical composite films, comprising large $(OA)_2(FA)_{n-1}Pb_nBr_{3n+1}$ microplatelets (0.5–2 μm) attached to $FAPbBr_3$ nanocrystals (*ca.* 5–30 nm). Ultra-smooth thin films (RMS ± 1 nm, for OA : $PbBr_2$ < 7 : 1) were achieved by spin-coating inks containing the preformed NCs and MPLs, and play a critical role in the realisation of these high performance films and devices. Under electrically driven conditions the 2D MPLs function as a transporting layer and as an intermediary to balance the electron and hole injection, while passivating the NCs. The excitons form in the higher bandgap (smaller) NCs and rapidly cascade into the lowest bandgap (largest) NCs within the size distribution. In the largest nanocrystals, the carrier densities increase substantially thereby reducing the chances of non-radiative recombination, delivering extremely high values of PLQY, EQE, luminance, power and current efficiencies. These hierarchical self-assemblies were transferred to different substrates, shown to be scalable to larger active diode areas, and present high feasibility of further development and continued improvements in performance. The levels of expansive high-performance luminescence metrics are unparalleled in the field of PeLEDs and compare rather favourably with state of the art multilayer green emitting OLEDs.[30]

Author contributions

X. Y. C, A. P., N. M., and S. G. M conceived the idea for the manuscript and designed the experiments. A. B., A. S. Z. L, and J. S. conducted the spectroscopic characterisation. X. Y. C, S. V., N. Y., A. P., B. C., and L. M. S prepared the samples and performed sample characterisation. V. C. performed the PLQY studies. A. B., S. V., N. Y., N. M., S. G. M., H. J. B., M. G., and C. S. analysed the data and wrote the manuscript. All authors discussed the results and commented on the manuscript at all stages. N. M. and S. G. M. led the project.

Conflicts of interest

There are no conflicts of interest to declare.

Acknowledgements

This research was supported by the National Research Foundation, Prime Minister's Office, Singapore under its Competitive Research Programme (CRP Award No. NRF-CRP14-2014-03) and through the Singapore–Berkeley Research Initiative for Sustainable Energy (SinBeRISE) CREATE Program. C. S and J. K. S. acknowledge support from the Singapore Ministry of Education (MOE2011-T3-1-005). H. J. B. acknowledges financial support from the European Union H2020 project SOLEDLIGHT (grant 643791), and the Spanish Ministry of Economy and Competitiveness (MINECO) *via* the Unidad de Excelencia María de Maeztu MDM-2015-0538 and MAT-2017-88821-R. L. M. S. acknowledges a predoctoral contract (FPI) from MINECO. M. G. acknowledges funding from the Swiss National Science foundation.

References

1 M. A. Green, A. Ho-Baillie and H. J. Snaith, *Nat. Photonics*, 2014, **8**, 506–514.
2 G. Xing, N. Mathews, S. S. Lim, N. Yantara, X. Liu, D. Sabba, M. Grätzel, S. Mhaisalkar and T. C. Sum, *Nat. Mater.*, 2014, **13**, 476–480.

3 Z.-K. Tan, R. S. Moghaddam, M. L. Lai, P. Docampo, R. Higler, F. Deschler, M. Price, A. Sadhanala, L. M. Pazos, D. Credgington, F. Hanusch, T. Bein, H. J. Snaith and R. H. Friend, *Nat. Nanotechnol.*, 2014, **9**, 687–692.
4 H. Cho, S.-H. Jeong, M.-H. Park, Y.-H. Kim, C. Wolf, C.-L. Lee, J. H. Heo, A. Sadhanala, N. Myoung, S. Yoo, S. H. Im, R. H. Friend and T.-W. Lee, *Science*, 2015, **350**, 1222–1225.
5 M. Saliba, T. Matsui, K. Domanski, J.-Y. Seo, A. Ummadisingu, S. M. Zakeeruddin, J.-P. Correa-Baena, W. R. Tress, A. Abate, A. Hagfeldt and M. Grätzel, *Science*, 2016, **354**, 206–209.
6 X. Y. Chin, D. Cortecchia, J. Yin, A. Bruno and C. Soci, *Nat. Commun.*, 2015, **6**, 7383.
7 M. Yuan, L. N. Quan, R. Comin, G. Walters, R. Sabatini, O. Voznyy, S. Hoogland, Y. Zhao, E. M. Beauregard, P. Kanjanaboos, Z. Lu, D. H. Kim and E. H. Sargent, *Nat. Nanotechnol.*, 2016, **11**, 872–877.
8 Z. Xiao, R. A. Kerner, L. Zhao, N. L. Tran, K. M. Lee, T.-W. Koh, G. D. Scholes and B. P. Rand, *Nat. Photonics*, 2017, **11**, 108–115.
9 H. Zhu, Y. Fu, F. Meng, X. Wu, Z. Gong, Q. Ding, M. V. Gustafsson, M. T. Trinh, S. Jin and X. Zhu, *Nat. Mater.*, 2015, **14**, 636–642.
10 S. A. Veldhuis, P. P. Boix, N. Yantara, M. Li, T. C. Sum, N. Mathews and S. G. Mhaisalkar, *Adv. Mater.*, 2016, **28**, 6804–6834.
11 N. Wang, L. Cheng, R. Ge, S. Zhang, Y. Miao, W. Zou, C. Yi, Y. Sun, Y. Cao, R. Yang, Y. Wei, Q. Guo, Y. Ke, M. Yu, Y. Jin, Y. Liu, Q. Ding, D. Di, L. Yang, G. Xing, H. Tian, C. Jin, F. Gao, R. H. Friend, J. Wang and W. Huang, *Nat. Photonics*, 2016, **10**, 699–704.
12 H. Zhang, S. Chen and X. W. Sun, *ACS Nano*, 2018, **12**, 697–704.
13 C.-Y. Kuei, W.-L. Tsai, B. Tong, M. Jiao, W.-K. Lee, Y. Chi, C.-C. Wu, S.-H. Liu, G.-H. Lee and P.-T. Chou, *Adv. Mater.*, 2016, **28**, 2795–2800.
14 J. Li, X. Shan, S. G. R. Bade, T. Geske, Q. Jiang, X. Yang and Z. Yu, *J. Phys. Chem. Lett.*, 2016, **7**, 4059–4066.
15 G. Xing, B. Wu, X. Wu, M. Li, B. Du, Q. Wei, J. Guo, E. K. L. Yeow, T. C. Sum and W. Huang, *Nat. Commun.*, 2017, **8**, 14558.
16 F. Zhang, H. Zhong, C. Chen, X.-g. Wu, X. Hu, H. Huang, J. Han, B. Zou and Y. Dong, *ACS Nano*, 2015, **9**, 4533–4542.
17 J.-H. Lee, S.-H. Cheng, S.-J. Yoo, H. Shin, J.-H. Chang, C.-I. Wu, K.-T. Wong and J.-J. Kim, *Adv. Funct. Mater.*, 2015, **25**, 361–366.
18 H. Sasabe, T. Chiba, S. J. Su, Y. J. Pu, K. Nakayama and J. Kido, *Chem. Commun.*, 2008, 5821–5823.
19 W. Y. Hung, G. C. Fang, S. W. Lin, S. H. Cheng, K. T. Wong, T. Y. Kuo and P. T. Chou, *Sci. Rep.*, 2014, **4**, 5161.
20 H. Sasabe, D. Tanaka, D. Yokoyama, T. Chiba, Y.-J. Pu, K.-i. Nakayama, M. Yokoyama and J. Kido, *Adv. Funct. Mater.*, 2011, **21**, 336–342.
21 L. N. Quan, Y. Zhao, F. P. Garcia de Arquer, R. Sabatini, G. Walters, O. Voznyy, R. Comin, Y. Li, J. Z. Fan, H. Tan, J. Pan, M. Yuan, O. M. Bakr, Z. Lu, D. H. Kim and E. H. Sargent, *Nano Lett.*, 2017, **17**, 3701–3709.
22 A. Laubsch, M. Sabathil, W. Bergbauer, M. Strassburg, H. Lugauer, M. Peter, S. Lutgen, N. Linder, K. Streubel, J. Hader, J. V. Moloney, B. Pasenow and S. W. Koch, *Phys. Status Solidi C*, 2009, **6**, S913–S916.
23 Y. C. Shen, G. O. Mueller, S. Watanabe, N. F. Gardner, A. Munkholm and M. R. Krames, *Appl. Phys. Lett.*, 2007, **91**, 141101.
24 M.-H. Kim, M. F. Schubert, Q. Dai, J. K. Kim, E. F. Schubert, J. Piprek and Y. Park, *Appl. Phys. Lett.*, 2007, **91**, 183507.
25 Y. Yang, X. A. Cao and C. H. Yan, *Appl. Phys. Lett.*, 2009, **94**, 041117.
26 K. J. Vampola, M. Iza, S. Keller, S. P. DenBaars and S. Nakamura, *Appl. Phys. Lett.*, 2009, **94**, 061116.
27 Y. Yang, X. A. Cao and C. Yan, *IEEE Trans. Electron Devices*, 2008, **55**, 1771–1775.
28 S. Gonzalez-Carrero, G. M. Espallargas, R. E. Galian and J. Perez-Prieto, *J. Mater. Chem. A*, 2015, **3**, 14039–14045.
29 L. C. Schmidt, A. Pertegás, S. González-Carrero, O. Malinkiewicz, S. Agouram, G. Mínguez Espallargas, H. J. Bolink, R. E. Galian and J. Pérez-Prieto, *J. Am. Chem. Soc.*, 2014, **136**, 850–853.
30 Y. Seino, S. Inomata, H. Sasabe, Y. J. Pu and J. Kido, *Adv. Mater.*, 2016, **28**, 2638–2643.